NANO LETTERS

pubs.acs.org/NanoLett Letter

Palladium Hydride Anchored on $SrTiO_3$ with Efficient Charge Separation and Surface Reaction Kinetics for Enhanced Photocatalytic Overall Water Splitting

Peng Cheng Ding,‖ Hai Xiang Yang,‖ Wen Bo Li, Yang Zhang, Hao Yang Lin, Meng Min Wang, Yu Yang Tang, Wen Jing Li, Hai Yang Yuan, Xue Lu Wang, Sheng Dai,* Peng Fei Liu,* and Hua Gui Yang*

Cite This: *Nano Lett.* 2025, 25, 6743−6752 Read Online

ACCESS | Metrics & More | Article Recommendations | Supporting Information

ABSTRACT: Cocatalyst engineering is critical for advancing photocatalysis, as it suppresses charge carrier recombination, promotes interfacial electron/hole extraction, and serves as active sites for redox reactions. However, the incompatibility existing between the cocatalyst and host photocatalyst, along with its intrinsic properties of active sites, limits further improvements in the charge separation, surface reaction kinetics, and overall performance. Herein, we introduce palladium hydrides (PdH_x) as an efficient cocatalyst on $SrTiO_3$ (STO) for photocatalytic overall water splitting, owing to their similar lattice parameters. The constructed PdH_x/STO demonstrates a remarkable 6.4-fold enhancement in hydrogen evolution compared to the Pd/STO control, reaching a rate of 5 $mmol \cdot g^{-1} \cdot h^{-1}$ at a stoichiometric H_2/O_2 ratio of 2:1. Structural characterizations and theoretical analyses prove that the *in situ* formed PdH_x sites feature the advantages of accelerated electron extraction and modulated hydrogen adsorption energies for hydrogen evolution; femtosecond transient absorption spectroscopy further reveals prolonged charge carrier lifetime and improved charge transfer efficiency.

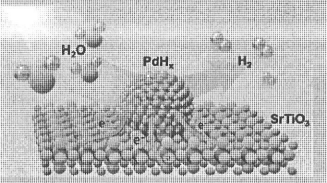

KEYWORDS: *Charge Carrier Dynamics, Hydrogen Adsorption Energy, Photocatalytic Overall Water Splitting, Palladium Hydride, $SrTiO_3$*

Photocatalytic overall water splitting (POWS) into hydrogen and oxygen offers an effective and sustainable solution to the pressing challenges of energy and environmental crises.[1,2] However, most photocatalysts exhibit insufficient charge carrier separation upon excitation, leading to significant recombination either within the bulk material or at the surface, which critically impairs their overall photocatalytic efficiency.[3] Various strategies have been proposed, including facet engineering,[4,5] doping (bandgap adjustment),[6] cocatalyst engineering,[1,7] and the construction of heterostructures.[8] Among these, cocatalyst engineering plays a paramount role, not only in facilitating efficient electron−hole pair separation but also in providing surface active sites for catalytic reactions.[9−14] Previous studies of cocatalysts have demonstrated that photocatalytic performance can be enhanced by modulating the atomic configuration (*e.g.*, nanoclusters, single-atom sites) or modifying the loading methods (e.g., photodeposition, impregnation). Nevertheless, the issue of structural compatibility between the host photocatalyst and cocatalyst is often overlooked when applying the aforementioned strategies. Specifically, the spatial distribution and interfacial alignment of the cocatalyst on the host photocatalyst may change, making it challenging to fundamentally understand their structural synergy and the mechanistic role of the cocatalyst.

Perovskite-type strontium titanate ($SrTiO_3$; STO) is a promising photocatalytic material for POWS.[1,2] Inspired by heterojunction cases with lattice-matched epitaxial growth,[15,16] we selected palladium (Pd) as cocatalyst for structural studies, guided by density functional theory (DFT) models. Pd shares similar lattice parameters with STO (Figure 1a), which may facilitate epitaxial deposition on STO with a lattice-matched interface.[17,18] Currently, Pd-based cocatalysts have been widely employed in total synthesis of natural products and large-scale industrial production.[19−24]

In photocatalysis, Pd-based cocatalysts excel in the selective hydrogenation of C═C and C═O bonds[25] and various organic synthesis,[26] attributed to their remarkable surface alloying characteristics and exceptional selectivity.[27] Unfortunately, metallic Pd sites exhibit suboptimal performance in hydrogen evolution reaction (HER), traditionally ascribed to strong hydrogen adsorption properties.[28,29] Despite the inherent limitations as an HER cocatalyst, the multifunctional

Received: February 13, 2025
Revised: April 5, 2025
Accepted: April 7, 2025
Published: April 15, 2025

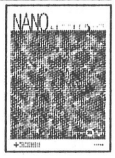

https://doi.org/10.1021/acs.nanolett.5c01007
Nano Lett. 2025, 25, 6743−6752

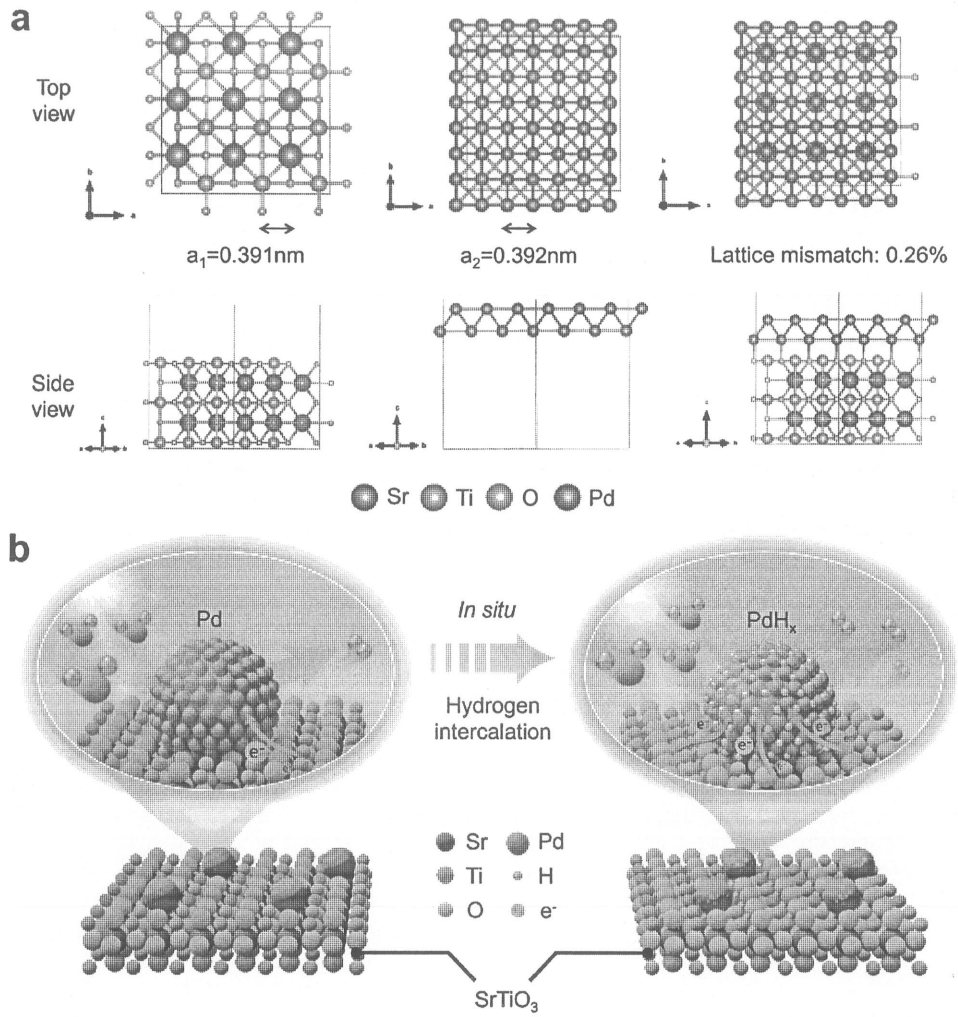

Figure 1. Atomic structure schematic of Pd cocatalyst loaded on the $SrTiO_3$ surface and schematic diagram of hydrogen intercalation process for the PdH_x/STO formation. (a) Crystal unit cell structures and constants of Pd and $SrTiO_3$, respectively, as well as the calculation of interfacial lattice mismatch. Note: The similarity in crystal structure between $SrTiO_3$ and Pd suggests the potential presence of a lattice matching effect, which may facilitate epitaxial growth. (b) Schematic illustration of *in situ* formed PdH_x cocatalysts on STO. Hydrogen intercalation enhances the electron enrichment capability of PdH_x sites and modulates their hydrogen desorption capacity, thereby boosting the POWS performance. *In situ* hydrogen intercalation ensures the spatial distribution and interfacial matching between the cocatalyst and the $SrTiO_3$ host photocatalyst remain consistent, enabling more precise exploration of the influence of the hydrogen intercalation for performance.

properties of Pd provide opportunities to enhance catalytic performance and further investigate the structure–activity relationships between the cocatalyst and the host photocatalyst. Notably, palladium hydride (PdH_x) is a solid-state phase formed by the intercalation of hydrogen atoms into the metallic palladium lattice, resulting in distinct physicochemical properties due to changes in both crystal structure and electronic configuration.[27,30] Its reversible phase transition and tunable electronic structure make it highly applicable in catalysis. Moreover, PdH_x demonstrates exceptional thermal stability and oxidation resistance, maintaining its lattice integrity without contraction even after annealing at 300 °C in an inert atmosphere or prolonged exposure to ambient air.[30]

Herein, we demonstrate that PdH_x is an efficient HER cocatalyst on STO with enhanced electron extraction ability and modulated hydrogen adsorption energy (see Figure 1b for the proposed schematic mechanism). The resultant PdH_x/STO achieves a hydrogen evolution rate up to 5 $mmol \cdot g^{-1} \cdot h^{-1}$ in a stoichiometric ratio of 2:1 for POWS, a remarkable 6.4-fold enhancement compared to Pd/STO, and maintains stable operation over 20 h. Our structural characterizations and theoretical calculations elucidate that the hydrogen intercalation process on Pd/STO successfully modulates the electronic structure of Pd without significantly changing the interfacial structures (Figure S1), which enhances interfacial electron transfer to PdH_x and promotes hydrogen desorption; femtosecond transient absorption (fs-TA) analysis reveals the advantages of PdH_x/STO in reaction kinetics and charge carrier transfer mechanisms. This work represents the first example of using Pd hydrides as HER cocatalyst in POWS and provides insights for deeply understanding and controllably tuning the cocatalyst at atomic scale to broaden cocatalyst functionality in other photocatalytic reactions.

The Al-doped STO photocatalyst was synthesized via a one-step molten salt method, while the PdH_x cocatalyst was introduced in a two-step process: first, a liquid-phase reduction

https://doi.org/10.1021/acs.nanolett.5c01007
Nano Lett. 2025, 25, 6743−6752

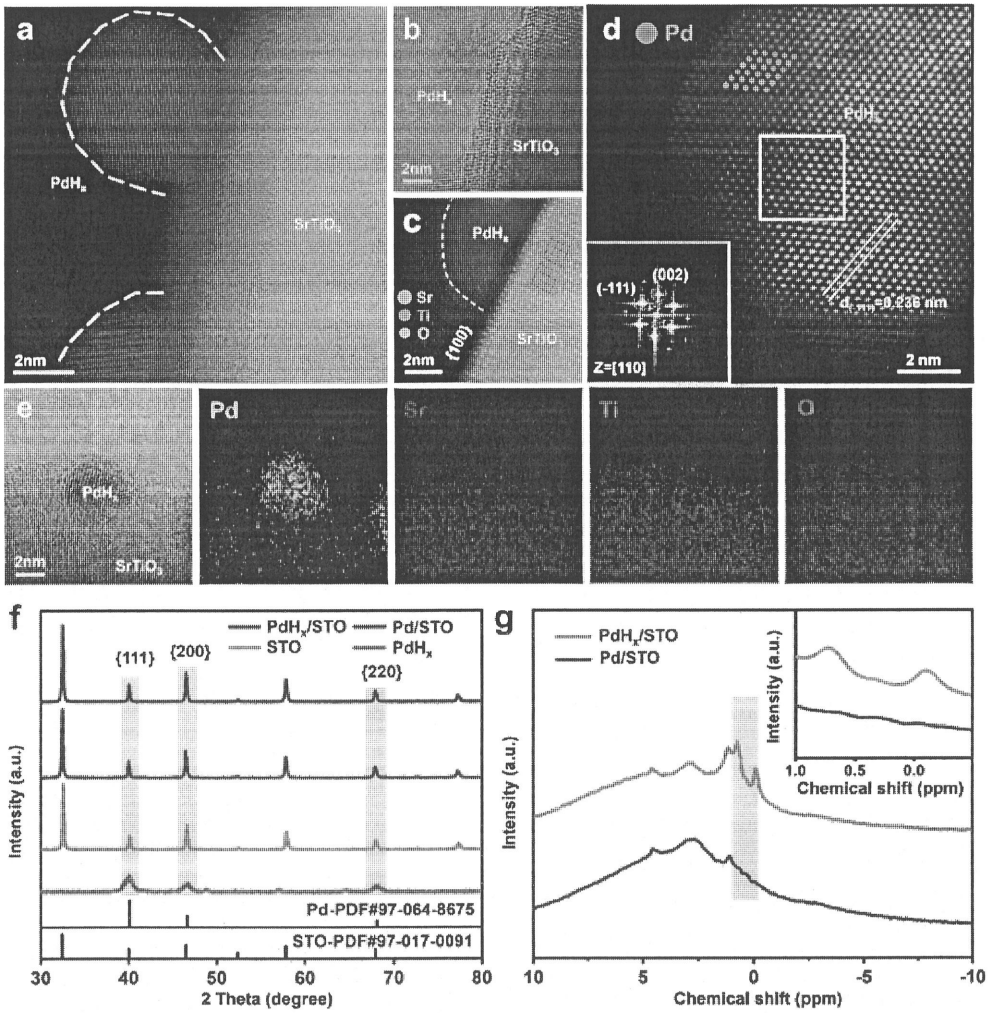

Figure 2. Crystalline structure and morphological characterization of PdH_x/STO. (a, b) HAADF- and BF-STEM images proving successful loading of PdH_x on STO. (c, d) Atomic-scale HAADF-STEM image of (c) PdH_x/STO and (d) PdH_x cocatalyst. Note: FFT pattern along the [110] zone axis of PdH_x in the white box line of (d), indicating the single-crystal structure of PdH_x. (e) HAADF-STEM image and the corresponding EDS elemental maps of PdH_x/STO. (f) XRD patterns of STO, Pd/STO (1.0 wt %), PdH_x/STO (1.0 wt %), and PdH_x. The orange shaded region represents the identical peak lines for Pd and STO. (g) SSNMR spectra of Pd/STO (1.0 wt %) and PdH_x/STO (1.0 wt %), providing detailed insights into the hydrogen-bonding components present in the photocatalysts. The two peak lines in the orange shaded region correspond to the Pd hydride peaks.

to load Pd nanoparticles, followed by hydrothermal hydrogen intercalation to form PdH_x *in situ*[18] (see details in the Supporting Information). High-angle annular dark-field scanning transmission electron microscopy (HAADF-STEM) images revealed that PdH_x was tightly bound to the surface of STO (Figures 2a-e and S2a-c). STEM-based energy-dispersive X-ray spectroscopy (EDS) elemental maps (Figures 2e and S2d) were used to examine the distribution of the catalyst components. The EDS analysis confirmed that STO exhibited a uniform distribution of Sr, Ti, and O elements with PdH_x nanoparticles clearly visible on the surface. Figures S3 and S4 showed that the STO was prepared with a cubic-octahedral structure composed of {100} and {111} crystal facets with Pd nanoparticles distributed uniformly across the surface. During the hydrogen intercalation process, PdH_x nanoparticles maintain their original distribution, and the intercalation has no discernible effect on the particle size of Pd (Figure S5). However, due to the effects of the high-temperature and high-pressure hydrothermal environment, the surface loading of the cocatalyst decreased by approximately 21−37%, as confirmed by inductively coupled plasma (ICP) spectroscopy (Table S1). Atomic-scale HAADF-STEM images (Figure 2c) revealed the well-defined {100} facet of the STO single crystal, which was loaded with PdH_x nanoparticles. Previous studies have shown that the {100} facet of STO is electron-rich under photocatalytic conditions, which facilitates reduction reactions. Therefore, the successful loading of PdH_x onto this facet provided ideal conditions for enhancing the hydrogen evolution reaction (HER) performance. Further atomic-scale HAADF-STEM images (Figure 2d) showed that the PdH_x nanoparticles exhibited well-defined crystal facets. But as shown in Figure 2d, interstitial hydrogen atoms were undetectable due to minimal electron scattering at high angles. However, lattice expansion associated with hydrogen intercalation was evident (Figures 2d and S3d), as demonstrated by the increased Pd−Pd distance (~2.36 Å along the ⟨110⟩

https://doi.org/10.1021/acs.nanolett.5c01007
Nano Lett. 2025, 25, 6743−6752

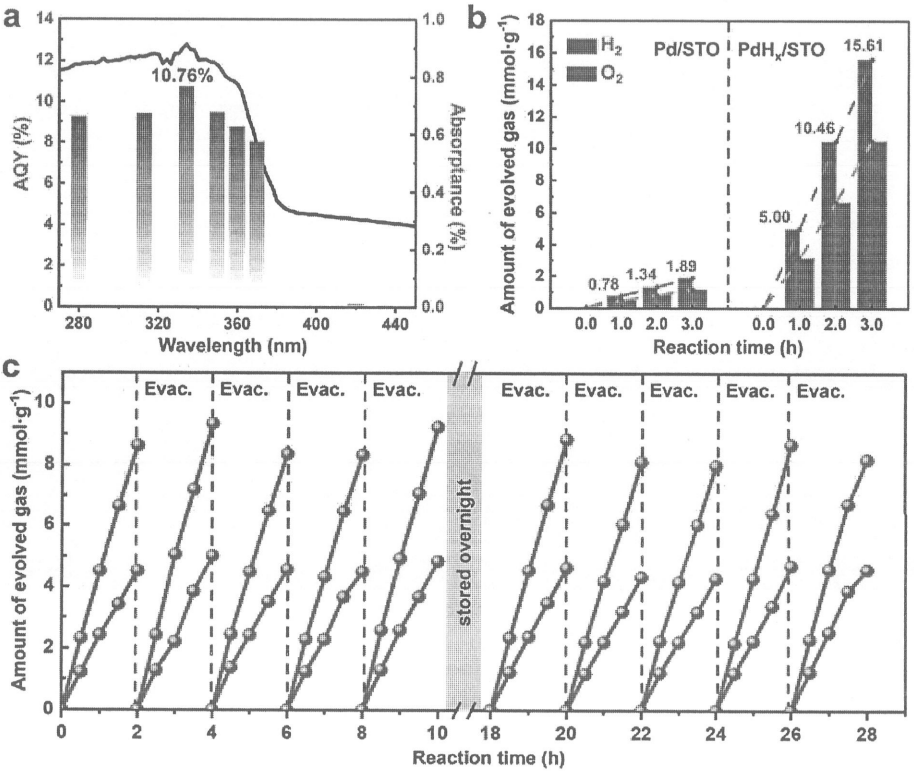

Figure 3. Photocatalytic overall water splitting performance. (a) The apparent quantum yield (AQY) of PdH_x/STO (1.0 wt %) plotted as a function of the wavelength of the incident light. (b) Time courses of gas evolution during overall water splitting over Pd/STO (1.0 wt %) and PdH_x/STO (1.0 wt %). (c) Stability test of PdH_x/STO (1.0 wt %) during photocatalytic water splitting. The produced H_2 and O_2 accumulated in the reaction system were evacuated every 2 h. The inner wall of the reactor window was cleaned after every evacuation. Reaction conditions: catalyst, 50 mg; reaction solution, 50 mL H_2O; light source, a 300 W Xe lamp (>300 nm). For the measurement of AQY, the 300 W Xe lamp was equipped with various band-pass filters.

directions) near the surface of PdH_x, compared to Pd (~2.29 Å). This lattice expansion corresponded to a 3−4% increase in the Pd lattice at the surface compared with Pd, serving as a robust indicator of hydrogen intercalation. Furthermore, the lattice place spacing of Pd/STO and PdH_x/STO provided preliminary estimates of lattice constants, as summarized in Table S2. The H-to-Pd ratio in PdH_x/STO (1.0 wt %) was approximately 0.51. Additionally, Figures 2d and S6 reveal that both STO and PdH_x nanoparticles exhibit single-crystal structures with high crystallinity, characterized by well-defined atomic facets and a highly ordered atomic arrangement extending from the surface into the bulk. Comparison of PDF standard cards for Pd (PDF#97-064-8675) and STO (PDF#97-017-0091) revealed that the Pd peaks, including {111}, {200}, and {220} reflections, appeared at 2θ values of 40.11°, 46.66°, and 68.12°, respectively. These peaks aligned well with the corresponding reflections of STO. X-ray diffraction (XRD) patterns confirmed consistent peak positions for Pd/STO, PdH_x/STO, and STO, with PdH_x matching three specific peaks (Figures 2f and S7). This similarity suggested a potential lattice-matching effect between the STO photocatalyst and the PdH_x cocatalyst, further supported by the orderly interfacial arrangement of STO, Pd, and PdH_x, forming a regular cross-like pattern (Figure S8) that was consistent with the alignment of peak reflections. Additionally, solid-state nuclear magnetic resonance (SSNMR) spectroscopy was used to investigate the hydrogen-bearing covalent bonds in the photocatalysts. Figure 2g showed the one-dimensional (1D) ^1H magic angle spinning (MAS) NMR spectra of the Pd/STO and PdH_x/STO samples, revealing two strong peaks at chemical shifts of −0.071 and 0.73 ppm, corresponding to hydrogen in the Pd hydride lattice.[28,31,32]

In a typical photocatalytic water splitting experiment, 50 mg of photocatalyst was dispersed in 50 mL of pure water, followed by sequential photodeposition of CoOOH as oxygen evolution catalyst (OEC) and Cr_2O_3 as overlayer covering on the PdH_x nanoparticles. As shown in Figure S9, we observed that the gas bubble generation rate for PdH_x/STO (1.0 wt %) was significantly more vigorous than that for Pd/STO (1.0 wt %). After evaluation of the photocatalytic activity for the POWS reaction, the H_2/O_2 ratio closely approached the stoichiometric ratio of 2:1 expected from water splitting. Photocatalytic H_2 evolution rates of PdH_x/STO enhanced significantly than that of Pd/STO (Figure 3b); notably, this enhancement was evident across various ranges of loadings. Figure S10 revealed that the gas evolution rate of PdH_x/STO ranged between 3 and 7 times that of Pd/STO under consistent feed ratios. Additionally, as shown in Figure S11, the POWS activity exhibited a volcano-like trend with varying PdH_x loadings, reaching peak activity at 1.0 wt % loading. At this point, the HER activity of PdH_x/STO was 6.4 times higher than that of Pd/STO (Figure 3b), achieving a hydrogen evolution rate of 5 $mmol \cdot g^{-1} \cdot h^{-1}$, representing a substantial improvement. Figure 3a shows the relationship between the apparent quantum yield (AQY) of the photocatalyst and the

https://doi.org/10.1021/acs.nanolett.5c01007
Nano Lett. 2025, 25, 6743−6752

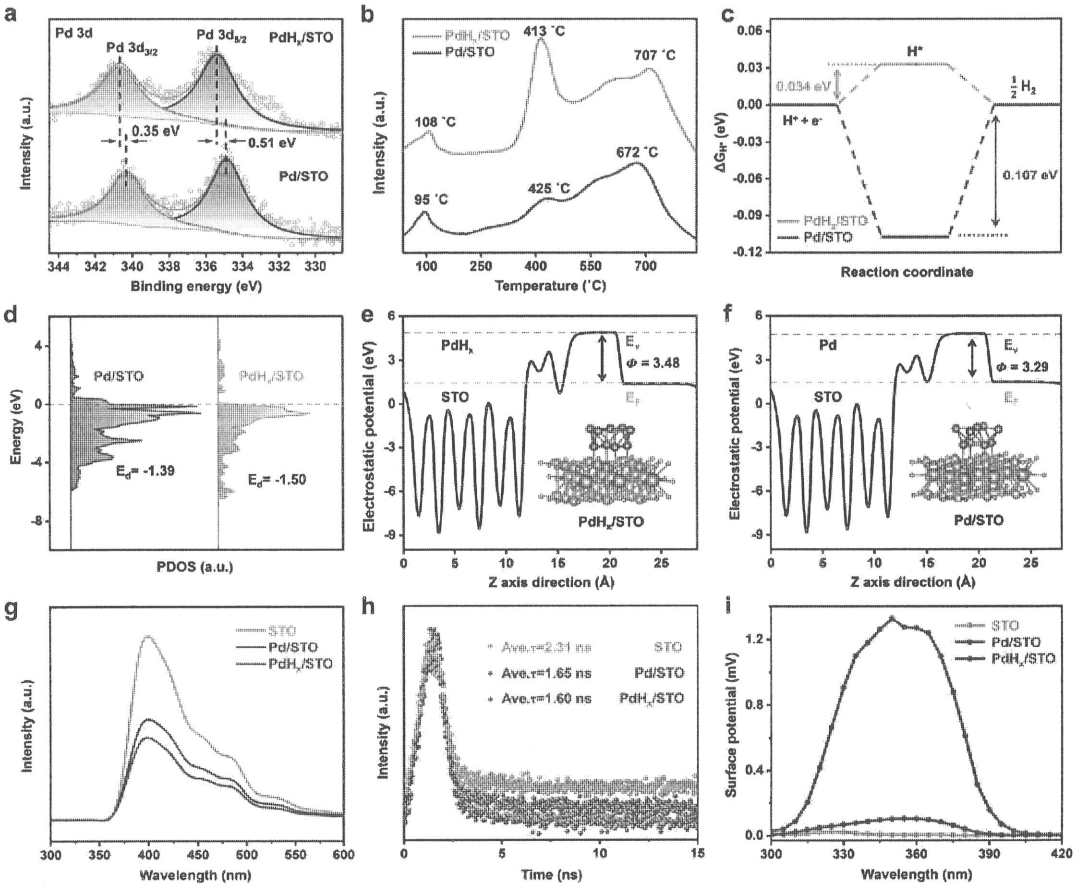

Figure 4. Analysis of electronic structure, surface properties, and behavior of photogenerated carriers in PdH_x/STO and controls. (a) XPS spectra of Pd 3d in Pd/STO and PdH_x/STO, demonstrating that hydrogen intercalation modulated the electronic structure of Pd. (b) H_2-TPD spectra of Pd/STO and PdH_x/STO. (c) DFT-calculated adsorption energies of H_{ads} on PdH_x/STO and Pd/STO. (d) Projected density of state (PDOS) of the d orbit of the Pd site on the surface of STO. (e, f) Calculated average potential profiles of (e) PdH_x and (f) Pd on STO, respectively. (g) PL spectra, (h) TR-PL spectra, and (i) surface photovoltage spectra of STO, Pd/STO (1.0 wt %), and PdH_x/STO (1.0 wt %), respectively, indicating that intercalation mitigated charge carrier recombination while it optimized the charge carrier migration dynamics.

irradiation wavelength during overall water splitting, with the efficiency reaching 10.76% at 334 nm (±10 nm), as shown in Table S3. Moreover, in POWS tests conducted over 28 h and 10 cycles, PdH_x/STO consistently maintained excellent activity, indicating the robust anchoring of PdH_x on the STO surface with high HER activity (Figure 3c).

To investigate the cause of the significant performance disparity, crystal structure characterization of the postreaction samples was conducted. TEM images revealed that after 20 h of testing, PdH_x remained firmly anchored, with Cr oxides serving as a protective layer to form a core−shell structure with PdH_x (Figure S12). As shown in Figures S13 and S14, the XRD patterns exhibited diffraction peaks that were consistent with those observed before the reaction. Moreover, the postreaction SSNMR spectra revealed two characteristic Pd hydride peaks at −0.41 and −0.29 ppm,[28,31,32] confirming that the crystal structure of the sample remained unchanged. Ultraviolet−visible diffuse reflectance spectroscopy (UV−vis DRS) in Figure S15 demonstrated a stable absorption edge at 384 nm for all samples, with an increase in background absorption observed above 400 nm. This increase was attributed to the progressively intensified tail absorption induced by the cocatalyst loading,[33] which was not expected to impact performance. Preliminary analysis, based on the Tauc equation, determined the optical band gaps of all samples to be approximately 3.24 eV (Figure S15), indicating that loading Pd or PdH_x as HER cocatalyst does not alter the intrinsic absorption edge of the STO.

X-ray photoelectron spectroscopy (XPS) was employed to investigate the valence states of Pd in Pd/STO and PdH_x/STO. Figures 4a and S16 displayed high-resolution spectra of the Pd 3d orbitals, showing the characteristic spin−orbit coupling doublet, $3d_{3/2}$ and $3d_{5/2}$, with an energy separation of 5.45 eV. Compared to Pd/STO, PdH_x/STO exhibited a 0.51 eV increase in binding energy, indicating electron transfer from palladium outward.[34,35] This shift resulted in a downward movement of the d-band center and an altered electronic structure postmodification. Consequently, the Pd species in PdH_x/STO were in an electron-deficient state, which may, to some extent, facilitate the accelerated transfer of photogenerated electrons. Notably, the cocatalyst loading had negligible impact on the oxidation states of Sr, Ti, and O, as confirmed by Figure S17. Moreover, the valence of Pd in PdH_x/STO remained unchanged before and after the reaction, whereas in Pd/STO, the peak at 336.8 eV observed after the reaction corresponds to Pd^{2+} (Figure S18), indicating that its electronic structure was altered due to the photocatalytic experiment.[40] This change aligned with the performance

https://doi.org/10.1021/acs.nanolett.5c01007
Nano Lett. 2025, 25, 6743−6752

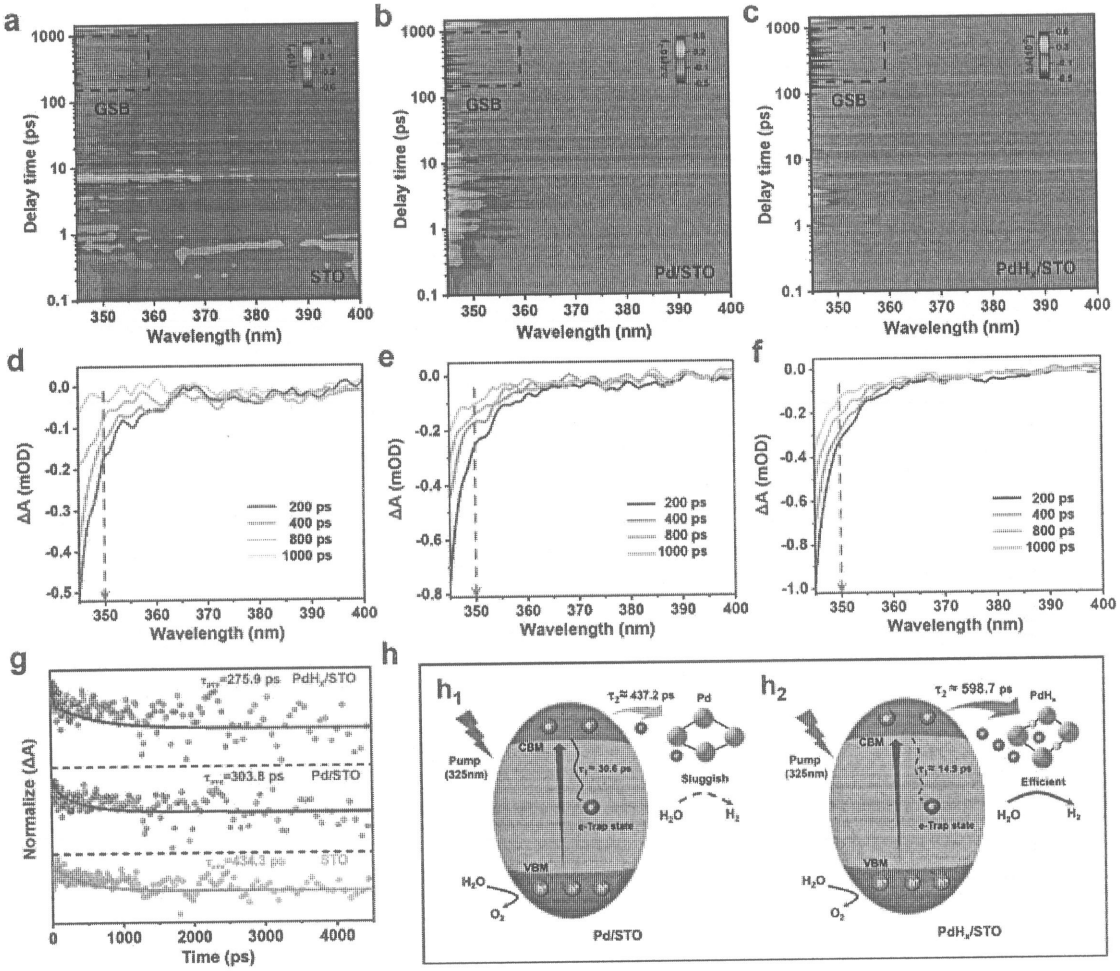

Figure 5. Photogenerated electron transfer mechanism and dynamics. (a-c) Pseudo color plots and (d, e) transient absorption spectra recorded at indicated delay times measured with 325 nm excitation for (a, d) STO, (b, e) Pd/STO (1.0 wt %), and (c, f) PdH_x/STO (1.0 wt %). Over the same period, the photogenerated charge carriers in PdH_x/STO sustain highest activity. (g) fs-TA kinetics probed near 350 nm and the corresponding multiexponential fits. (h) Schematic diagrams for the enhanced interfacial transfer of photogenerated electrons after hydrogen intercalation. The charge carriers in PdH_x/STO exhibit the most efficient lifetime. (h_1) and (h_2) correspond to Pd/STO (1.0 wt %) and PdH_x/STO (1.0 wt %), respectively.

degradation observed in the three h test (Figure 3b), further suggesting that hydrogen intercalation not only modulated the electronic structure of Pd but also maintained the stability of the PdH_x sites. To evaluate the interaction between reactant molecules and the photocatalyst surfaces, hydrogen temperature-programmed desorption (H_2-TPD) was performed (Figure 4b), and the desorption peak near 100 °C corresponded to physisorbed hydrogen, while peaks between 410 and 430 °C were attributed to chemisorbed hydrogen desorbing from Pd or PdH_x sites. The desorption peak reflected the amount of gas desorbed, and PdH_x/STO exhibited the highest desorption among all samples. This observation showed that PdH_x sites facilitate hydrogen desorption, suggesting that hydrogen intercalation mitigated the strong hydrogen adsorption typically associated with Pd.[36−38]

DFT calculations were conducted to further investigate the active sites (details were provided in the Supporting Information). We constructed a trilayer STO {100} model featuring a Pd cluster and PdH_x species on its surface, with hydrogen atoms incorporated into the Pd cluster to simulate a PdH_x composition with a 2:1 stoichiometry (Figure S19). As shown in Figure 4c, the hydrogen adsorption energies at the Pd sites were evaluated before and after hydrogen incorporation. PdH_x/STO exhibited a weaker hydrogen adsorption energy (ΔG = 0.03 eV). In contrast, Pd sites in Pd/STO showed relatively stronger hydrogen adsorption (ΔG = −0.11 eV), indicating that hydrogen intercalation effectively weakens the bond between Pd and the hydrogen adsorbates. The projected density of states (PDOS) analysis revealed substantial electronic structure discrepancies of Pd sites between the Pd/STO and PdH_x/STO surfaces. As illustrated in Figure 4d, the Pd site on PdH_x/STO showed a lower electron density around the Fermi level compared to the Pd site on Pd/STO. This result indicated that hydrogen incorporation reduces the electron density on the PdH_x surface, diminishing the direct electronic interaction between the Pd site and hydrogen adsorbates, which ultimately weakened hydrogen adsorption. Moreover, the theoretical results demonstrated that PdH_x exhibited enhanced electron extraction capabilities and elevated carrier mobility. Work function analysis of Pd and PdH_x deposited on STO revealed

https://doi.org/10.1021/acs.nanolett.5c01007
Nano Lett. 2025, 25, 6743−6752

that PdH_x, with a work function of 3.48 eV, interacted more strongly with STO surface than Pd clusters (3.29 eV) (Figure 4e,f). This superior electron transfer capability of PdH_x highlighted its important role in driving the surface reactivity. Electrochemical impedance spectroscopy (EIS) measurements revealed similar Nyquist plot diameters for all samples (Figure S20), as summarized in Table S4. As shown in Figure S21, linear sweep voltammetry (LSV) curves showed that PdH_x/STO had the lowest overpotential for HER, indicating that HER was thermodynamically most favorable on PdH_x/STO.[39,40] To further investigate the behavior of photogenerated charge carriers, transient photocurrent response measurements were performed. Figure S22 shows that the chopped photocurrents of PdH_x/STO were significantly higher than those of Pd/STO, which was consistent with their performance. Steady-state photoluminescence (PL) and time-resolved photoluminescence (TR-PL) spectra were conducted to evaluate the recombination rate and effective lifetime of carriers. As shown in Figure 4g, the fluorescence intensity was highest for STO, followed by that for Pd/STO, with PdH_x/STO exhibiting the lowest intensity. This trend suggested that PdH_x/STO minimizes charge recombination and maximizes the carrier utilization efficiency. Similarly, the carrier lifetimes (Figure 4h) were shortest for PdH_x/STO (1.60 ns), followed by Pd/STO (1.65 ns), and longest for STO (2.31 ns), indicating that PdH_x/STO exhibited the most efficient charge transport. In terms of evaluating spatial charge separation capabilities, surface photovoltage (SPV) measurements were conducted on these samples.[41,42] Under illumination (300–400 nm), the SPV values for PdH_x/STO were significantly higher than those for Pd/STO and STO (Figure 4i), indicating that PdH_x/STO exhibited a markedly higher carrier concentration at the surface under operational conditions, which highlighted the enhanced space charge separation promoted by PdH_x.

In photocatalytic processes, charge carrier separation and migration were highly intricate and transient, occurring on ultrafast time scales such as femtoseconds and picoseconds. To further investigate the dynamics and mechanisms of charge transfer facilitated by Pd and PdH_x cocatalysts, the carrier dynamics of these photocatalytic systems were monitored in real time using femtosecond time-resolved transient absorption (fs-TA) spectroscopy. Upon excitation with a 325 nm pump, all pre- and postreaction fs-TA spectra exhibited a continuous absorption peak in the 345–365 nm range (Figure 5a-f). This signal was predominantly attributed to ground-state bleaching (GSB) of the STO substrate, as the loading of Pd-based cocatalysts was relatively low (~1.0 wt %).[43] Notably, the GSB peak for PdH_x/STO decayed more slowly over time compared to Pd/STO, demonstrating higher photogenerated charge activity in PdH_x/STO. The prolonged retention of photogenerated electrons in the conduction band (CB) of STO in the presence of PdH_x, compared to Pd alone,[44,45] indicated that PdH_x served as an effective cocatalyst. This enhancement in charge transfer to STO helps to explain the superior water-splitting performance observed in the PdH_x/STO systems.

In addition, excited-state dynamics of all samples were analyzed by fitting the fs-TA kinetics at 350 nm using an exponential decay function, with detailed fitting parameters provided in Table S5. The average relaxation lifetimes for STO, Pd/STO, and PdH_x/STO were 434.3, 303.8, and 275.9 ps, respectively (Figure 5g). This trend aligned with the average lifetimes observed in time-resolved photoluminescence (TR-PL) measurements (Figure 4h), confirming the efficient charge carrier transport in these systems.[46] According to literature, in cocatalyst/host catalyst systems, τ_1 corresponds to the charge recombination process from the excited state (ES) to the trap state (TS), while τ_2 represents the charge transfer process from the ES in the catalyst to the cocatalyst (e.g., charge transfer from STO to the surface of Pd or PdH_x).[47] Comparison of τ_1 and τ_2 between the samples showed that in PdH_x/STO, the τ_1 relaxation lifetime was not only shorter than in Pd/STO but also significantly prolonged (Figure 5h). This result suggested that hydrogen intercalation enhanced the functionality of Pd as cocatalyst by reducing the trapping of photogenerated electrons by defect states, while also significantly facilitating their transfer to active sites that were conducive to catalytic reactions.[48] Consequently, hydrogen intercalation was crucial for improving the kinetics of catalytic reactions in Pd/STO systems to enhance the overall performance. The aforementioned characterization results indicated that atomic-scale modulation of the cocatalysts, such as intercalating Pd with appropriate heteroatoms such as hydrogen, can significantly facilitate charge transfer and inhibit the recombination of photogenerated electrons and holes, which in turn dramatically improves the POWS performance.

In this work, we have developed Pd hydrides as HER cocatalysts on STO for enhanced photocatalytic overall water splitting. The *in situ* formation of PdH_x via hydrogen intercalation not only accelerates the electron extraction to the cocatalyst but also weakens the hydrogen bonding energy for the optimized HER kinetics, verified by spectroscopic characterizations and theoretical calculations. The hydrogen intercalation optimizes the compatibility between Pd and STO, and the constructed PdH_x/STO demonstrates a remarkable hydrogen evolution rate of 5 $mmol \cdot g^{-1} \cdot h^{-1}$, representing a 6.4-fold enhancement compared to the pristine Pd/STO, while maintaining stable operation for over 20 h. We highlight this is the first implement of Pd hydrides used as HER cocatalyst in POWS, and the performance might be further enhanced by *in situ*, controllable modulation of the electronic structure of the loaded cocatalyst to optimize compatibility with the host catalyst. This work provides fundamental insights into the atomic-level understanding of the cocatalyst effect and sheds light on precise exploration of cocatalyst functionality for other photocatalytic reactions.

■ ASSOCIATED CONTENT

Supporting Information

The Supporting Information is available free of charge at https://pubs.acs.org/doi/10.1021/acs.nanolett.5c01007.

Detailed experimental and computational methods, figures and tables showing TEM characterization, the XPS result, the ICP-OES result, DFT calculations, photocatalytic performances and electrochemical performances of catalysts (PDF)

■ AUTHOR INFORMATION

Corresponding Authors

Sheng Dai – *Key Laboratory for Advanced Materials and Feringa Nobel Prize Scientist Joint Research Centre, School of Chemistry and Molecular Engineering, East China University of Science & Technology, Shanghai 200237, China*;
Email: shengdai@ecust.edu.cn

https://doi.org/10.1021/acs.nanolett.5c01007
Nano Lett. 2025, 25, 6743–6752

Peng Fei Liu – *Key Laboratory for Ultrafine Materials of Ministry of Education, Shanghai Engineering Research Center of Hierarchical Nanomaterials, School of Materials Science and Engineering, East China University of Science and Technology, 200237 Shanghai, China;* orcid.org/0000-0003-0411-0488; Email: pfliu@ecust.edu.cn

Hua Gui Yang – *Key Laboratory for Ultrafine Materials of Ministry of Education, Shanghai Engineering Research Center of Hierarchical Nanomaterials, School of Materials Science and Engineering, East China University of Science and Technology, 200237 Shanghai, China;* orcid.org/0000-0003-0436-8622; Email: hgyang@ecust.edu.cn

Authors

Peng Cheng Ding – *Key Laboratory for Ultrafine Materials of Ministry of Education, Shanghai Engineering Research Center of Hierarchical Nanomaterials, School of Materials Science and Engineering, East China University of Science and Technology, 200237 Shanghai, China*

Hai Xiang Yang – *Key Laboratory for Ultrafine Materials of Ministry of Education, Shanghai Engineering Research Center of Hierarchical Nanomaterials, School of Materials Science and Engineering, East China University of Science and Technology, 200237 Shanghai, China*

Wen Bo Li – *Key Laboratory for Advanced Materials and Feringa Nobel Prize Scientist Joint Research Centre, School of Chemistry and Molecular Engineering, East China University of Science & Technology, Shanghai 200237, China*

Yang Zhang – *Key Laboratory for Ultrafine Materials of Ministry of Education, Shanghai Engineering Research Center of Hierarchical Nanomaterials, School of Materials Science and Engineering, East China University of Science and Technology, 200237 Shanghai, China*

Hao Yang Lin – *Key Laboratory for Ultrafine Materials of Ministry of Education, Shanghai Engineering Research Center of Hierarchical Nanomaterials, School of Materials Science and Engineering, East China University of Science and Technology, 200237 Shanghai, China*

Meng Min Wang – *Key Laboratory for Ultrafine Materials of Ministry of Education, Shanghai Engineering Research Center of Hierarchical Nanomaterials, School of Materials Science and Engineering, East China University of Science and Technology, 200237 Shanghai, China*

Yu Yang Tang – *Key Laboratory for Ultrafine Materials of Ministry of Education, Shanghai Engineering Research Center of Hierarchical Nanomaterials, School of Materials Science and Engineering, East China University of Science and Technology, 200237 Shanghai, China*

Wen Jing Li – *Key Laboratory for Ultrafine Materials of Ministry of Education, Shanghai Engineering Research Center of Hierarchical Nanomaterials, School of Materials Science and Engineering, East China University of Science and Technology, 200237 Shanghai, China*

Hai Yang Yuan – *Key Laboratory for Ultrafine Materials of Ministry of Education, Shanghai Engineering Research Center of Hierarchical Nanomaterials, School of Materials Science and Engineering, East China University of Science and Technology, 200237 Shanghai, China;* orcid.org/0000-0001-6175-391X

Xue Lu Wang – *Physics Department & Shanghai Key Laboratory of Magnetic Resonance, School of Physics and Electronic Science, East China Normal University, Shanghai 200241, China;* orcid.org/0000-0001-5096-5159

Complete contact information is available at: https://pubs.acs.org/10.1021/acs.nanolett.5c01007

Author Contributions

‖(P.-C.D. and H.-X.Y.) These authors contributed equally to this work.

Notes

The authors declare no competing financial interest.

■ ACKNOWLEDGMENTS

This work was financially supported by the National Key Research and Development Program of China (No. 2023YFA1507102), the National Natural Science Foundation of China (22239001, 51920105003, and 22376062), the Shanghai Pilot Program for Basic Research (22TQ1400100-12), the Science and Technology Commission of Shanghai Municipality (21DZ1207101 and 22ZR1415700), and the Fundamental Research Funds for the Central Universities. The authors also thank Shanghai Aitins Technology Co., Ltd. for their support and assistance in first-principles calculations. The authors also thank the Frontiers Science Center for Materiobiology and Dynamic Chemistry.

■ REFERENCES

(1) Takata, T.; Jiang, J.; Sakata, Y.; Nakabayashi, M.; Shibata, N.; Nandal, V.; Seki, K.; Hisatomi, T.; Domen, K. Photocatalytic water splitting with a quantum efficiency of almost unity. *Nature* **2020**, *581*, 411–414.

(2) Nishiyama, H.; Yamada, T.; Nakabayashi, M.; Maehara, Y.; Yamaguchi, M.; Kuromiya, Y.; Nagatsuma, Y.; Tokudome, H.; Akiyama, S.; Watanabe, T.; Narushima, R.; Okunaka, S.; Shibata, N.; Takata, T.; Hisatomi, T.; Domen, K. Photocatalytic solar hydrogen production from water on a 100 m^2 scale. *Nature* **2021**, *598*, 304–307.

(3) Yang, J.; Wang, D.; Han, H.; Li, C.; et al. Roles of Cocatalysts in Photocatalysis and Photoelectrocatalysis. *Acc. Chem. Res.* **2013**, *46*, 1900–1909.

(4) Yang, H. G.; Sun, C. H.; Qiao, S. Z.; Zou, J.; Liu, G.; Smith, S. C.; Cheng, H. M.; Lu, G. Q. Anatase TiO_2 single crystals with a large percentage of reactive facets. *Nature* **2008**, *453*, 638–641.

(5) Zhang, Y.; Wu, X.; Wang, Z. H.; Peng, Y.; Liu, Y.; Yang, S.; Sun, C.; Xu, X.; Zhang, X.; Kang, J.; Wei, S. H.; Liu, P. F.; Dai, S.; Yang, H. G. Crystal Facet Engineering on $SrTiO_3$ Enhances Photocatalytic Overall Water Splitting. *J. Am. Chem. Soc.* **2024**, *146*, 6618–6627.

(6) Bao, Y.; Zou, H.; Du, S.; Xin, X.; Wang, S.; Shao, G.; Zhang, F. Metallic Powder Promotes Nitridation Kinetics for Facile Synthesis of (Oxy)Nitride Photocatalysts. *Adv. Mater.* **2023**, *35*, No. 2302276.

(7) Kraeutler, B.; Bard, A. J. Heterogeneous Photocatalytic Preparation of Supported Catalysts. Photodeposition of Platinum on TiO_2 Powder and Other Substrates. *J. Am. Chem. Soc.* **1978**, *100*, 4317–4318.

(8) Zhang, Y.; Li, Y.; Xin, X.; Wang, Y.; Guo, P.; Wang, R.; Wang, B.; Huang, W.; Sobrido, A. J.; Li, X. Internal quantum efficiency higher than 100% achieved by combining doping and quantum effects for photocatalytic overall water splitting. *Nat. Energy* **2023**, *8*, 504–514.

(9) Ran, J.; Zhang, J.; Yu, J.; Jaroniec, M.; Qiao, S. Z. Earth-abundant cocatalysts for semiconductorbased photocatalytic water splitting. *Chem. Soc. Rev.* **2014**, *43*, 7787–7812.

(10) Xing, J.; Jiang, H. B.; Chen, J. F.; Li, Y. H.; Wu, L.; Yang, S.; Zheng, L. R.; Wang, H. F.; Hu, P.; Zhao, H. J.; Yang, H. G. Active sites on hydrogen evolution photocatalyst. *J. Mater. Chem. A* **2013**, *1*, 15258.

(11) Qi, Y.; Zhang, J.; Kong, Y.; Zhao, Y.; Chen, S.; Li, D.; Liu, W.; Chen, Y.; Xie, T.; Cui, J.; Li, C.; Domen, K.; Zhang, F. Unraveling of

cocatalysts photodeposited selectively on facets of $BiVO_4$ to boost solar water splitting. *Nat. Commun.* **2022**, *13*, 484.
(12) Li, Y. H.; Liu, P. F.; Pan, L. F.; Wang, H. F.; Yang, Z. Z.; Zheng, L. R.; Hu, P.; Zhao, H. J.; Gu, L.; Yang, H. G. Local atomic structure modulations activate metal oxide as electrocatalyst for hydrogen evolution in acidic water. *Nat. Commun.* **2015**, *6*, 8064.
(13) Liu, Y.; Wang, L. J.; Zhang, H.; Yuan, H. Y.; Zhang, Q.; Gu, L.; Wang, H. F.; Hu, P.; Liu, P. F.; Jiang, Z.; Yang, H. G. Boosting Photocatalytic Water Oxidation Over Bifunctional Rh^0 -Rh^{3+} Sites. *Angew. Chem., Int. Ed.* **2021**, *60*, 22761−22768.
(14) Zhang, X.; Gao, D.; Zhu, B.; Cheng, B.; Yu, J.; Yu, H. Enhancing photocatalytic H_2O_2 production with Au co-catalysts through electronic structure modification. *Nat. Commun.* **2024**, *15*, 3212.
(15) Tian, J.; Zhang, Y.; Shi, Z.; Liu, Z.; Zhao, Z.; Li, J.; Li, N.; Huang, H. Enabling Interfacial Lattice Matching by Selective Epitaxial Growth of CuS Crystals on Bi_2WO_6 Nanosheets for Efficient CO_2 Photoreduction into Solar Fuels. *Angew. Chem., Int. Ed.* **2025**, *64*, No. e202418496.
(16) Hu, J.; Li, B.; Li, X.; Yang, T.; Yang, X.; Qu, J.; Cai, Y.; Yang, H.; Lin, Z. Lattice Match-Enabled Covalent Heterointerfaces with Built-in Electric Field for Efficient Hydrogen Peroxide Photosynthesis. *Adv. Mater.* **2024**, *36*, No. 2412070.
(17) Ham, Y.; Hisatomi, T.; Goto, Y.; Moriya, Y.; Sakata, Y.; Yamakata, A.; Kubota, J.; Domen, K. Flux-mediated doping of $SrTiO_3$ photocatalysts for efficient overall water splitting. *J. Mater. Chem. A* **2016**, *4*, 3027−3033.
(18) Zhu, Y.; Gao, C.; Bai, S.; Chen, S.; Long, R.; Song, L.; Li, Z.; Xiong, Y. Hydriding Pd cocatalysts: An approach to giant enhancement on photocatalytic CO_2 reduction into CH_4. *Nano Res.* **2017**, *10*, 3396−3406.
(19) Yan, J. L.; Hu, L.; Lu, Y.; Yu, J. Q. Catalyst-Controlled Chemoselective γ-C(sp^3)−H Lactonization of Carboxylic Acid: Methyl versus Methylene. *J. Am. Chem. Soc.* **2024**, *146*, 29311−29314.
(20) Pramanick, P. K.; Zhao, S.; Ji, H. T.; Chen, X.; Yang, G. Pd(II)-Catalyzed Asymmetric [2 + 2] Annulation for the Construction of Chiral Benzocyclobutenes. *Angew. Chem., Int. Ed.* **2025**, *64*, No. e202415927.
(21) Fan, H.; Yang, Q. Q.; Fang, S. R.; Xu, Y. N.; Lv, Y.; Lin, H. Y.; Lin, M. Y.; Liu, J. K.; Wu, Y. X.; Yuan, H. Y.; Dai, S.; Liu, P. F.; Yang, H. G. Operando Stable Palladium Hydride Nanoclusters Anchored on Tungsten Carbides Mediate Reverse Hydrogen Spillover for Hydrogen Evolution. *Angew. Chem., Int. Ed.* **2024**, *63*, No. e202412080.
(22) He, X.; Zhang, H.; Zhang, X.; Zhang, Y.; He, Q.; Chen, H.; Cheng, Y.; Peng, M.; Qin, X.; Ji, H.; Ma, D. Building up libraries and production line for single atom catalysts with precursor-atomization strategy. *Nat. Commun.* **2022**, *13*, 5721.
(23) Johansson Seechurn, C. C.; Kitching, M. O.; Colacot, T. J.; Snieckus, V. Palladium-Catalyzed Cross-Coupling: A Historical Contextual Perspective to the 2010 Nobel Prize. *Angew. Chem., Int. Ed.* **2012**, *51*, 5062−5085.
(24) Littke, A. F.; Fu, G. C. A Convenient and General Method for Pd-Catalyzed Suzuki Cross-Couplings of Aryl Chlorides and Arylboronic Acids. *Angew. Chem., Int. Ed.* **1998**, *37*, 3387−3388.
(25) Qin, T.; Cornella, J.; Li, C.; Malins, L. R.; Edwards, J. T.; Kawamura, S.; Maxwell, B. D.; Eastgate, M. D.; Baran, P. S. A general alkyl-alkyl cross-coupling enabled by redox-active esters and alkylzinc reagents. *Science* **2016**, *352* (6287), 801−805.
(26) Gao, Z.; Montini, T.; Mu, J.; Luo, N.; Fonda, E.; Fornasiero, P.; Wang, F. Photocatalytic Methanol Dehydrogenation Promoted Synergistically by Atomically Dispersed Pd and Clustered Pd. *J. Am. Chem. Soc.* **2024**, *146*, 24440−24449.
(27) Jia, Y.; Huang, T. H.; Lin, S.; Guo, L.; Yu, Y. M.; Wang, J. H.; Wang, K. W.; Dai, S. Stable Pd−Cu Hydride Catalyst for Efficient Hydrogen Evolution. *Nano Lett.* **2022**, *22*, 1391−1397.
(28) Li, G.; Kobayashi, H.; Taylor, J. M.; Ikeda, R.; Kubota, Y.; Kato, K.; Takata, M.; Yamamoto, T.; Toh, S.; Matsumura, S.; Kitagawa, H. Hydrogen storage in Pd nanocrystals covered with a metal−organic framework. *Nat. Mater.* **2014**, *13*, 802−806.
(29) Maeda, K.; Teramura, K.; Saito, N.; Inoue, Y.; Domen, K. Improvement of photocatalytic activity of $(Ga_{1-x}Zn_x)(N_{1-x}O_x)$ solid solution for overall water splitting by co-loading Cr and another transition metal. *J. Catal.* **2006**, *243*, 303−308.
(30) Zhao, Z.; Huang, X.; Li, M.; Wang, G.; Lee, C.; Zhu, E.; Duan, X.; Huang, Y. Synthesis of Stable Shape-Controlled Catalytically Active β-Palladium Hydride. *J. Am. Chem. Soc.* **2015**, *137*, 15672−15675.
(31) Polisset, M.; Fraissard, J. ^1H NMR study of hydrogen adsorption on Pd-NaY: influence of metal particle size. *Colloids Surf. A Physicochem. Eng. Asp.* **1993**, *72*, 197−206.
(32) Mete, E.; Yilmaz, B.; Uner, D. PdH α-phase is associated with residual oxygen as revealed by *in situ* ^1H NMR measurements and DFT-NMR estimations. *Appl. Surf. Sci.* **2023**, *641*, No. 158421.
(33) Luo, L.; Fu, L.; Liu, H.; Xu, Y.; Xing, J.; Chang, C. R.; Yang, D. Y.; Tang, J. Synergy of Pd atoms and oxygen vacancies on In_2O_3 for methane conversion under visible light. *Nat. Commun.* **2022**, *13*, 2930.
(34) Li, H.; Zeng, R.; Feng, X.; Wang, H.; Xu, W.; Lu, X.; Xie, Z.; Abruna, H. D. Oxidative Stability Matters: A Case Study of Palladium Hydride Nanosheets for Alkaline Fuel Cells. *J. Am. Chem. Soc.* **2022**, *144*, 8106−8114.
(35) Xu, W.; Fan, G.; Chen, J.; Li, J.; Zhang, L.; Zhu, S.; Su, X.; Cheng, F.; Chen, J. Nanoporous Palladium Hydride for Electrocatalytic N_2 under Ambient Conditions. *Angew. Chem., Int. Ed.* **2020**, *59*, 3511−3516.
(36) Deng, X.; Zhang, J.; Qi, K.; Liang, G.; Xu, F.; Yu, J. Ultrafast electron transfer at the In_2O_3/Nb_2O_5 S-scheme interface for CO_2 photoreduction. *Nat. Commun.* **2024**, *15*, 4807.
(37) Wang, S.; Ge, B.; Yang, Z.; Zhang, H.; Yang, Q.; Hu, C.; Bao, X.; Yuan, P. Construction of Highly Active Pd−Ti^{3+} Sites in Defective Pd/TiO_2 Catalysts for Efficient Hydrogenation of Styrene−Butadiene−Styrene. *ACS Catal.* **2024**, *14*, 1432−1442.
(38) Zhang, J.; Pan, Y.; Feng, D.; Cui, L.; Zhao, S.; Hu, J.; Wang, S.; Qin, Y. Mechanistic Insight into the Synergy between Platinum Single Atom and Cluster Dual Active Sites Boosting Photocatalytic Hydrogen Evolution. *Adv. Mater.* **2023**, *35*, No. 2300902.
(39) Zu, D.; Ying, Y.; Wei, Q.; Xiong, P.; Ahmed, M. S.; Lin, Z.; Li, M. M.; Li, M.; Xu, Z.; Chen, G.; Bai, L.; She, S.; Tsang, Y. H.; Huang, H. Oxygen Vacancies Trigger Rapid Charge Transport Channels at the Engineered Interface of S-Scheme Heterojunction for Boosting Photocatalytic Performance. *Angew. Chem., Int. Ed.* **2024**, *63*, No. e202405756.
(40) Wang, L.; Li, Y.; Ai, Y.; Fan, E.; Zhang, F.; Zhang, W.; Shao, G.; Zhang, P. Tracking Heterogeneous Interface Charge Reverse Separation in $SrTiO_3$/NiO/NiS Nanofibers with In Situ Irradiation XPS. *Adv. Funct. Mater.* **2023**, *33*, No. 2306466.
(41) Peng, Y.; Zhang, Y.; Wang, X.; Sui, X. Y.; Lin, M. Y.; Zhu, Y.; Jing, C.; Yuan, H. Y.; Yang, S.; Liu, P. F.; Dai, S.; Zheng, Z.; Yang, H. G.; Hou, Y. Polar Aromatic Two-dimensional Dion-Jacobson Halide Perovskites for Efficient Photocatalytic H_2 Evolution. *Angew. Chem., Int. Ed.* **2024**, *63*, No. e202319882.
(42) Chen, R.; Fan, F.; Dittrich, T.; Li, C. Imaging photogenerated charge carriers on surfaces and interfaces of photocatalysts with surface photovoltage microscopy. *Chem. Soc. Rev.* **2018**, *47*, 8238−8262.
(43) Wang, H.; Zhang, X.; Zhang, W.; Zhou, M.; Jiang, H. L. Heteroatom-Doped Ag_{25} Nanoclusters Encapsulated in Metal−Organic Frameworks for Photocatalytic Hydrogen Production. *Angew. Chem., Int. Ed.* **2024**, *63*, No. e202401443.
(44) Wu, K.; Zhu, H.; Liu, Z.; Rodríguez-Córdoba, W.; Lian, T. Ultrafast Charge Separation and Long-Lived Charge Separated State in Photocatalytic CdS−Pt Nanorod Heterostructures. *J. Am. Chem. Soc.* **2012**, *134*, 10337−10340.
(45) Wang, L.; Zhang, J.; Yu, H.; Patir, I. H.; Li, Y.; Wageh, S.; Al-Ghamdi, A. A.; Yu, J. Dynamics of Photogenerated Charge Carriers in Inorganic/Organic S-Scheme Heterojunctions. *J. Phys. Chem. Lett.* **2022**, *13*, 4695−4700.

https://doi.org/10.1021/acs.nanolett.5c01007
Nano Lett. 2025, 25, 6743−6752

(46) Godin, R.; Wang, Y.; Zwijnenburg, M. A.; Tang, J.; Durrant, J. R. Time-Resolved Spectroscopic Investigation of Charge Trapping in Carbon Nitrides Photocatalysts for Hydrogen Generation. *J. Am. Chem. Soc.* **2017**, *139*, 5216−5224.
(47) Qiu, B.; Cai, L.; Zhang, N.; Tao, X.; Chai, Y. A Ternary Dumbbell Structure with Spatially Separated Catalytic Sites for Photocatalytic Overall Water Splitting. *Adv. Sci.* **2020**, *7*, No. 1903568.
(48) He, B.; Xiao, P.; Wan, S.; Zhang, J.; Chen, T.; Zhang, L.; Yu, J. Rapid Charge Transfer Endowed by Interfacial Ni-O Bonding in Sscheme Heterojunction for Efficient Photocatalytic H_2 and Imine Production. *Angew. Chem., Int. Ed.* **2023**, *62*, No. e202313172.

https://doi.org/10.1021/acs.nanolett.5c01007
Nano Lett. 2025, 25, 6743−6752